

Article

Active Regulation of Electromagnetic Force in Wireless Power Transfer Systems

Yandong Hu ^{1,2,3}, Wenbo Dong ^{1,2,3,*} , Xiang Li ^{1,2}, Hanxun Zhang ^{1,2,3} and Liangzhi Men ^{1,2}

¹ Technology and Engineering Center for Space Utilization, Chinese Academy of Sciences, Beijing 100094, China; huyandong20@csu.ac.cn (Y.H.); johu@csu.ac.cn (X.L.); zhanghanxun@csu.ac.cn (H.Z.); menliangzhi13@163.com (L.M.)

² Key Laboratory of Space Utilization, Chinese Academy of Sciences, Beijing 100094, China

³ University of Chinese Academy of Sciences, Beijing 100049, China

* Correspondence: wbdong@csu.ac.cn

Abstract: To reduce the interference from the electromagnetic force caused by coupling coils due to distance changes in a wireless power transfer (WPT) system, this paper conducts a theoretical analysis of the factors influencing the electromagnetic force experienced by the receiving coil. Maxwell electromagnetic simulation is used for modeling and analysis, revealing the trends in the electromagnetic force exerted on the receiving coil. Based on this analysis, a method is proposed that actively adjusts the working frequency of WPT to alter the current phases of the transmitting and receiving coils, thereby regulating the magnitude of the force on the receiving coil. Finally, mechanical tests, including torque experiments, were conducted to validate the proposed method. The electromagnetic force on the coil in the microgravity isolation platform of a space station was reduced from 961 μN to 113 μN , a level which plays an important role in improving the microgravity index of the system.

Keywords: wireless power transfer (WPT); electromagnetic force; frequency adjustment; microgravity isolation platform



Citation: Hu, Y.; Dong, W.; Li, X.; Zhang, H.; Men, L. Active Regulation of Electromagnetic Force in Wireless Power Transfer Systems. *Electronics* **2024**, *13*, 1568. <https://doi.org/10.3390/electronics13081568>

Academic Editor: Niamat Hussain

Received: 20 March 2024

Revised: 13 April 2024

Accepted: 16 April 2024

Published: 19 April 2024



Copyright: © 2024 by the authors. Licensee MDPI, Basel, Switzerland. This article is an open access article distributed under the terms and conditions of the Creative Commons Attribution (CC BY) license (<https://creativecommons.org/licenses/by/4.0/>).

1. Introduction

Wireless power transfer (WPT) technology utilizes principles from electrical engineering, power electronics, and control theory, combining media such as magnetic fields, electric fields, and microwaves to achieve non-contact transmission of electrical energy [1–4]. This technology overcomes the limitations of fixed positions in traditional wired power transmission, eliminates the risks associated with friction and electrical contact, and enhances the flexibility and safety of systems. Currently, WPT has found widespread applications in electric vehicles, consumer electronics, and the aerospace industry, gradually maturing as a technology.

The Chinese space station has deployed a number of important scientific facilities, both inside and outside the modules, to support a wide range of space science experiments, including space life science and technology, microgravity fluid physics, microgravity combustion science, space materials science, and microgravity fundamental physics [5–8]. Among these, the levitating experiment platform in the high microgravity cabinet is a key apparatus for creating a high microgravity environment. It isolates various external disturbances by controlling its attitude and position through jet propulsion and is equipped with an electromagnetic levitation experiment platform for installation of scientific payloads.

As shown in Figure 1, the levitating experiment platform adopts a square structure with a highly integrated design concept. It mainly consists of components such as the experimental bench main control unit, WPT, MEMS micro-thruster, intermittent gas supply system, main power line, payload and camera. In order to power the levitating experiment system, the high microgravity experiment cabinet adopts WPT technology, replacing the potential hazards associated with traditional umbilical cord power supply processes. The

transmitting coil for WPT is fixed on the high microgravity cabinet, while the receiving coil is dependent on the levitation device. This configuration enables contactless and force-free transmission.

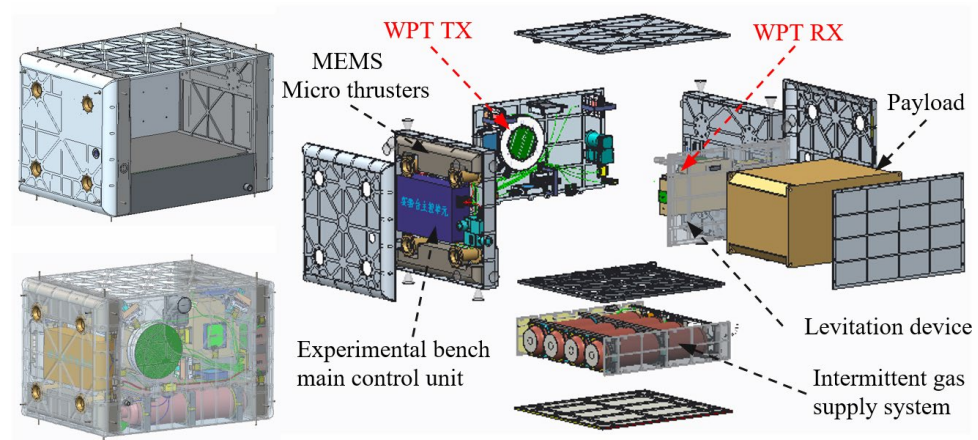


Figure 1. Schematic layout diagram of the levitating experiment platform.

The WPT technology operates on the principle of electromagnetic induction, enabling the levitation device to draw energy from the induced current within the transmitting coil. However, during the process of electric power transmission, the high-frequency alternating magnetic field generated by the transmitting coil can interfere with the receiving coil, creating electromagnetic-force disturbances. This interference poses a significant challenge, especially for the suspension device inside the high-precision experiment cabinet, which requires an extremely stringent mechanical testing environment. Therefore, employing WPT technology to energize the levitation device within the high microgravity experiment cabinet also generates the influence of electromagnetic-force.

In order to define the microgravity requirements of the space-science experimental payloads, the vibration isolation performance requirements of the experimental payload platform are shown in Table 1. The actuator of the controlled platform needs to generate sufficient main power in time to suppress the vibration of its platform.

Table 1. The parameters of experimental payloads.

Project	MAIS	Ultra Microgravity Experiment Payloads	Output (After Control)
Noise	45 mN umbilical cable	0 ~ 500 μ N	Null
Max output force	250 mN	Null	0 ~ 800 μ N
Load weight	\geq 12 kg	\geq 45 kg	\geq 45 kg
Load power	\geq 20 W	\geq 85 W	\geq 85 W
Free path	\geq 10 \times 10 mm	\geq 30 \times 30 mm	\geq 50 \times 50 mm

At present, in the field of WPT, the focus has predominantly been on harnessing electromagnetic-forces for various applications, with comparatively limited emphasis on mitigating electromagnetic-force interference.

Studies in the literature [9,10] propose a design scheme for miniature robots based on WPT technology. By adjusting the size of the receiving coil capacitor, the intensity and direction of electromagnetic-force can be precisely controlled, thereby achieving precise control of the robot’s steering and speed. The team further suggests the use of interleaved DC coils to power the miniature robot [11,12], controlling the thrust generated by the miniature robot by adjusting the current in the external DC power coil. Study [13] achieves simultaneous control by electromagnetic-force of multiple robots by using the frequency splitting phenomenon. By setting the operating frequency of the receiving coil to the

splitting frequency of the transmitting coil, it is possible to independently control the motion of each miniature robot. Additionally, by adjusting the parameters of the transmitting coil, the number of miniature robots can be increased or decreased. Studies [14,15] use finite element methods to analyze and calculate the uniformity of the magnetic field generated by the Helmholtz coil or Maxwell coil used, successfully achieving control over the motion direction of the receiving robots and reducing motion errors by using position feedback. Studies [16–19] propose a structural electromagnetic-force smoothing method based on phase difference control. By adjusting the adjustable branch inductance connected in series with a certain branch of the transmitting coil, control over the phase of the current flowing through the coupled coil is achieved. Studies [20,21] propose a method of using a closed magnetic core instead of two open magnetic cores, converting the original electromagnetic attractive force between the two cores into an internal force, and thereby eliminating the influence of an external electromagnetic attraction force.

The present study aims to mitigate the impact of electromagnetic-force on the receiving coil. Theoretical analysis of the coil’s force situation is conducted to identify the primary factors influencing the magnitude of the electromagnetic-force. Finally, a method is proposed to control the electromagnetic-force on the receiving coil by real-time adjustment of the switching frequency. Through simulation and experimentation, it is found that effective control of the electromagnetic-force on the receiving coil is achieved when the transmission distance varies. This validates the correctness of the proposed concept and establishes a theoretical basis and experimental evidence for the application of WPT technology in space stations.

2. Calculation and Analysis of Electromagnetic Forces in Coupling Coils

As mentioned above, the electromagnetic-force on the current-carrying conductor is generated due to the interaction between the magnetic field and the electric current. In order to study the electromagnetic-force characteristics of the coupled coils in WPT systems, the current characteristics of the system are analyzed deeply. Figure 2 shows the mutual inductance model of a loosely coupled transformer.

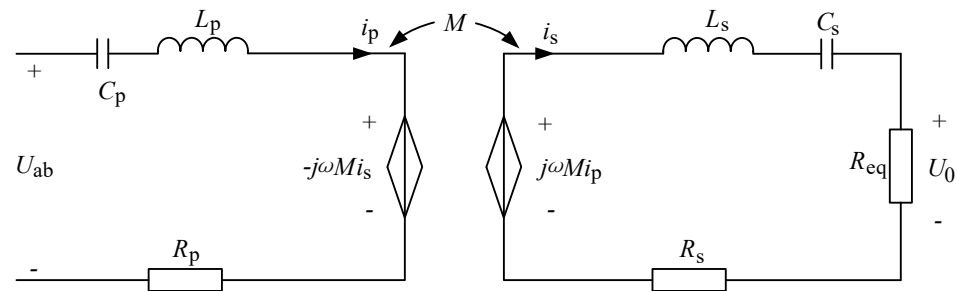


Figure 2. Series–series compensated topology of the WPT system.

Figure 2 illustrates the most basic series–series compensated topology of the WPT system, in which U_{ab} represents the voltage across the terminals of the transmitting coil, M is the mutual inductance between the two coils, R_{eq} is the load, I_p and I_s are the effective values of the currents in the transmitting and receiving coils, R_p and R_s are the internal resistances of the two coils, L_p and L_s are the self-inductances of the transmitting and receiving coils, C_p and C_s are the compensation capacitors for the transmitting and receiving coils and ω is the switching angular frequency of the inverter.

According to the Kirchhoff’s Voltage Law (KVL) equation,

$$\begin{cases} \left(R_p + j\omega L_p + \frac{1}{j\omega C_p} \right) I_p - j\omega M I_s = U_{ab} \\ \left(R_{eq} + R_s + j\omega L_s + \frac{1}{j\omega C_s} \right) I_s - j\omega M I_p = 0 \end{cases} \quad (1)$$

The current I_s in the receiving coil is obtained as follows:

$$I_s = \frac{j\omega M}{\left(R_{eq} + R_s + j\omega L_s + \frac{1}{j\omega C_s}\right)} I_p \tag{2}$$

$$I_s = I_p \frac{\omega M}{\sqrt{(R_s + R_{eq})^2 + \left(\omega L_s - \frac{1}{\omega C_s}\right)^2}} \angle \varphi \tag{3}$$

$$\varphi = \tan^{-1} \frac{\omega L_s - \frac{1}{\omega C_s}}{R_s + R_{eq}} \tag{4}$$

where φ is the phase difference between i_p and i_s .

It is assumed that

$$i_p = I_p \sin \omega t \tag{5}$$

$$i_s = I_s \sin(\omega t + \varphi) \tag{6}$$

The magnetic force [22] between the two current-carrying coils can be derived from the general expression for their mutual inductance:

$$F = I_p I_s \frac{\partial M}{\partial Z_Q} \tag{7}$$

where Z_Q is the generalized coordinate. The magnetic force has only an axial component because the coils are coaxial. We will begin with the current element of the receiving coil.

The amperage force F of the current element $i_s d\vec{l}$ on the coil L_s is

$$dF = i_s d\vec{l} \times \vec{B}_p = i_s r_s d(\phi \cdot \vec{e}_\phi) \times \vec{B}_p \tag{8}$$

\vec{B}_p represents the electromagnetic induction intensity at the location of the current element, r_s is the radius of the receiving coil and ϕ is the angular radian of the current element.

Using cylindrical coordinates, the vector \vec{B}_p is decomposed as follows:

$$\vec{B}_p = B_z \vec{e}_z + B_\rho \vec{e}_\rho + B_\phi \vec{e}_\phi \tag{9}$$

Then,

$$dF = i_s r_s d(\phi \cdot \vec{e}_\phi) \times (B_z \vec{e}_z + B_\rho \vec{e}_\rho + B_\phi \vec{e}_\phi) \tag{10}$$

where $B_z, B_\rho, B_\phi, \vec{e}_z, \vec{e}_\rho, \vec{e}_\phi$ is the column coordinate decomposition of electromagnetic induction and ϕ radian, respectively.

Since the current is in the direction $\phi, B_\phi = 0$.

$$dF = i_s r_s d(\phi \cdot \vec{e}_\phi) \times (B_z \vec{e}_z + B_\rho \vec{e}_\rho) = i_s r_s B_z d(\phi \cdot \vec{e}_\rho) - i_s r_s B_\rho d(\phi \cdot \vec{e}_z) \tag{11}$$

Among them,

$$F_\rho = \oint i_s r_s B_z d(\phi \cdot \vec{e}_\rho) \tag{12}$$

$$F_z = \oint i_s r_s B_\rho d(\phi \cdot \vec{e}_z) = 2\pi i_s r_s B_\rho \tag{13}$$

The magnetic induction intensity of the location of the B_ρ current element is stimulated by the current of the sending end.

Because of

$$B = \mu H \tag{14}$$

$$\nabla \times H = J + \frac{\partial D}{\partial t} \tag{15}$$

B is produced by I_p , and they have the same phase.

Therefore,

$$B_\rho = B \cdot \sin \omega t \tag{16}$$

The electromagnetic-force of the receiving coil is obtained as follows.

$$F_z = 2\pi i_s r_s B_\rho = 2\pi r_s B I_s \sin(\omega t + \varphi) \sin \omega t = \pi r_s B I_s [\cos \varphi - \cos(2\omega t + \varphi)] \tag{17}$$

The electromagnetic-force on the receiving end of the multi-turn coil is

$$F_z = F_{z_dc} - F_{z_ac} \tag{18}$$

where

$$F_{z_ac} = \frac{N\pi r_s \omega M I_p B \cos(2\omega t + \varphi)}{\sqrt{(R_s + R_{eq})^2 + \left(\omega L_s - \frac{1}{\omega C_s}\right)^2}} \tag{19}$$

$$F_{z_dc} = \frac{N\pi r_s \omega M I_p B \cos \varphi}{\sqrt{(R_s + R_{eq})^2 + \left(\omega L_s - \frac{1}{\omega C_s}\right)^2}} \tag{20}$$

According to the above formula, the electromagnetic-force on the receiving coil consists of high-frequency alternating-current force F_{z_ac} and direct-current bias force F_{z_dc} . The high-frequency alternating-current force does not contribute propulsion to the coupling mechanism, while the direct-current bias force is non-cancelable and exerts a persistent influence on the coupling mechanism. In order to mitigate the impact of electromagnetic interference on the levitator system, the study focuses solely on the research of the direct-current bias force F_{z_dc} .

3. Active Regulation Methods for Electromagnetic Force

Assume that the frequency of the resonant cavity at the receiver is f_s , the switching frequency of the system is f , and the transmission distance is h .

According to Equation (20), the electromagnetic-force F_{z_dc} is mainly affected by the current I_p in the transmitting coil, mutual inductance M , operating angular frequency ω , and the phase difference φ between the currents. The phase difference φ directly determines the magnitude and direction of the electromagnetic-force.

The levitation system's free-drifting state leads to changes in the relative positions of the receiving and transmitting coils, which affects the resonant relationship of the coupling coil. In this case, the current phase difference $\varphi \neq 90^\circ$, resulting in electromagnetic-force interference.

The specific rationale is as follows:

- (1) When h is kept at the rated position,

$$f = f_s \tag{21}$$

The receiving end exhibits purely resistive characteristics, and the current phase difference $\varphi = 90^\circ$, $\cos \varphi = 0$ and the electromagnetic-force ($F_{z_dc} = 0$) on the receiving coil is zero. Consequently, there is no static force between the two coils.

- (2) When h increases,

$$h \uparrow \rightarrow L_s \downarrow \rightarrow f_s \uparrow \tag{22}$$

Then,

$$f < f_s \tag{23}$$

At this time, the receiving end exhibits capacitive characteristics, and the current phase difference $\varphi > 90^\circ$, leading to $\cos\varphi < 0$. The electromagnetic-force $F_{z_dc} < 0$ on the receiving coil, resulting in an attractive force between the two coils.

If the fixed frequency operating mode is adopted, the receiving end will be drawn closer until a repulsive force is generated. In ideal conditions, it would undergo oscillations back and forth until equilibrium is reached at $f = f_s$. However, in reality, interference may cause the equilibrium point to deviate. Additionally, during the attraction process, the proximity may lead to overvoltage protection in the subsequent DC/DC stage.

If a variable frequency operating mode is adopted, as the transmission distance increases, the operating frequency is reduced to adjust the magnitude of the current phase difference φ , maintaining it near 90° . This ensures that the electromagnetic-force on the receiving end is minimized.

(3) When h decreases,

$$h \downarrow \rightarrow L_s \uparrow \rightarrow f_s \downarrow \tag{24}$$

Then,

$$f > f_s \tag{25}$$

At this time, the receiving end exhibits inductive characteristics, and the current phase difference $\varphi < 90^\circ$, leading to $\cos\varphi > 0$. The electromagnetic-force $F_{z_dc} > 0$ on the receiving coil, resulting in a repulsive force between the two coils.

If the fixed frequency operating mode is adopted, the receiving end will be pushed away until an attractive force is generated. In ideal conditions, it would oscillate back and forth until equilibrium is reached at $f = f_s$. However, in reality, interference may cause the equilibrium point to deviate. Additionally, during the repulsion process, the distance may become too great, leading to power loss.

If a variable frequency operating mode is adopted, as the transmission distance decreases, the operating frequency is increased to adjust the magnitude of the current phase difference φ , maintaining it around 90° . This ensures that the electromagnetic-force on the receiving end is minimized.

Figure 3 is a flowchart of frequency control. When the transmission distance changes, adjusting the system’s switching frequency alters the phase difference φ to minimize the electromagnetic-force on the receiving coil. To measure the position changes of the receiving coil, three sets of laser ranging sensors are employed. Each set measures one degree of freedom of the coil’s position, providing changes in the coil’s motion along the x , y and z axes. The position data obtained from the receiving laser displacement sensor provides the position x , y , z of the coil during motion.

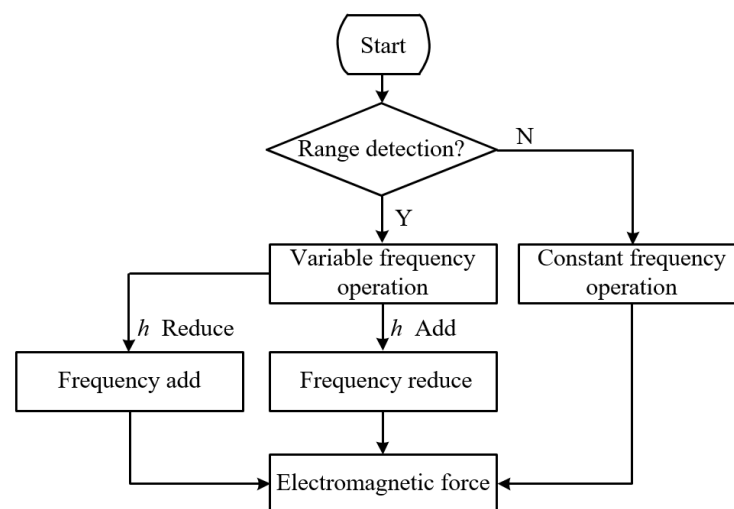


Figure 3. Flowchart of frequency control.

Figure 4 below illustrates the frequency tracking control diagram for WPT. The frequency tracking adjustment system mainly consists of laser ranging sensors, current sampling circuits, zero-crossing comparators, DPLL (digital phase-locked loop), and driver circuits. The specific implementation process is as described in the following.

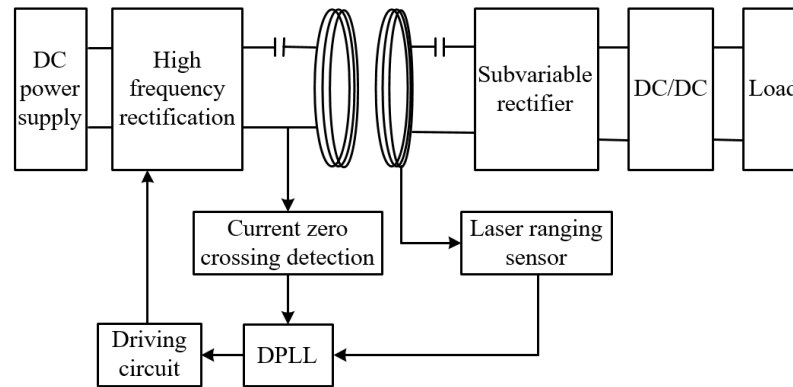


Figure 4. Frequency tracking control diagram.

The laser ranging sensor continuously detects the position of the receiving coil in real time and sends the collected position information to the FPGA to adjust the system’s operating frequency. The current-sensing circuit continuously samples the current i_p flowing through the transmitting coil. Subsequently, this current is processed by zero-crossing comparison circuits to generate square wave signals u_{ab} that are in phase and frequency with i_p . The DPLL compares u_{ab} with the feedback-driven signal u_0 , generating a driving logic signal at the same frequency as u_{ab} . Finally, this driving logic signal enters the driver circuit to produce four-channel PWM waveforms to control the switching transistors.

The paper adopts a frequency tracking control method based on a PI-controlled digital phase-locked loop (DPLL). To facilitate the study and determination of the impact of the proportional K_P and integral K_I parameters of the internal loop filter of the PI-control digital phase-locked loop on frequency adjustment, it is necessary to establish its mathematical model. Figure 5 illustrates the flowchart of the mathematical model of the PI-controlled digital phase-locked loop.

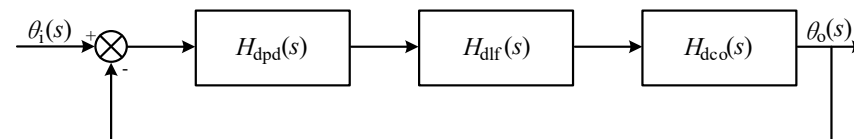


Figure 5. Mathematical model of the PI-controlled phase-locked loop.

In the diagram above, $\theta_i(s)$ denotes the phase of the input signal u_i , while $\theta_o(s)$ represents the phase of the output signal u_o . Additionally, $H_{dpd}(s)$, $H_{dlf}(s)$, and $H_{dco}(s)$ correspond to the transfer functions of the phase detector, loop filter, and voltage-controlled oscillator (VCO), respectively.

$$H_{dpd}(s) = \frac{f_{clk}}{2\pi f} \tag{26}$$

where f_{clk} represents the system clock frequency, and f denotes the frequency of the input signal.

The transfer function of a loop filter with proportional and integral characteristics, essentially a PI controller, can be represented as follows:

$$H_{dlf}(s) = K_P + \frac{K_I f}{s} \tag{27}$$

where K_P and K_I represent the proportional and integral coefficients of the loop filter, respectively.

Near the lock frequency point, the transfer function of the voltage-controlled oscillator (VCO) equals the rate of change of the output phase $\theta_o(s)$ with respect to its input division ratio N . Therefore, the transfer function of the frequency divider can be expressed as

$$H_{dco}(s) = \frac{\partial \theta_o}{\partial N} = -\frac{\pi f_{clk}}{N^2 s} \tag{28}$$

Therefore, the transfer function of the system near the lock frequency point can be obtained as follows:

$$H_{DPLL}(s) = \frac{\frac{K_P f_{clk}^2}{2N^2 f} s + \frac{K_I f_{clk}^2}{2N^2}}{s^2 + \frac{K_P f_{clk}^2}{2N^2 f} s + \frac{K_I f_{clk}^2}{2N^2}} \tag{29}$$

In the local dynamic model, when the input signal varies around the lock frequency point such that $f \approx f_o \approx f_{clk}/2N$, the transfer function can be simplified as

$$H_{DPLL}(s) = \frac{2K_P f_i \cdot s + 2K_I f^2}{s^2 + 2K_P f_i \cdot s + 2K_I f^2} \tag{30}$$

From Equation (30), it can be observed that the system is a typical second-order system. According to the general form of a second-order system transfer function, the damping ratio ζ and natural frequency ω_c of the system can be obtained as follows:

$$\omega_c = \frac{K_P}{\sqrt{2K_I}} \tag{31}$$

$$\zeta = \sqrt{2K_I f_i} \tag{32}$$

With $f = 100$ kHz as the assumed input signal frequency, the dynamic performance of the DPLL solely depends on the parameters K_P and K_I of the loop filter when the input signal is constant. The impacts of different values of K_P and K_I on the system performance are illustrated in Figure 6.

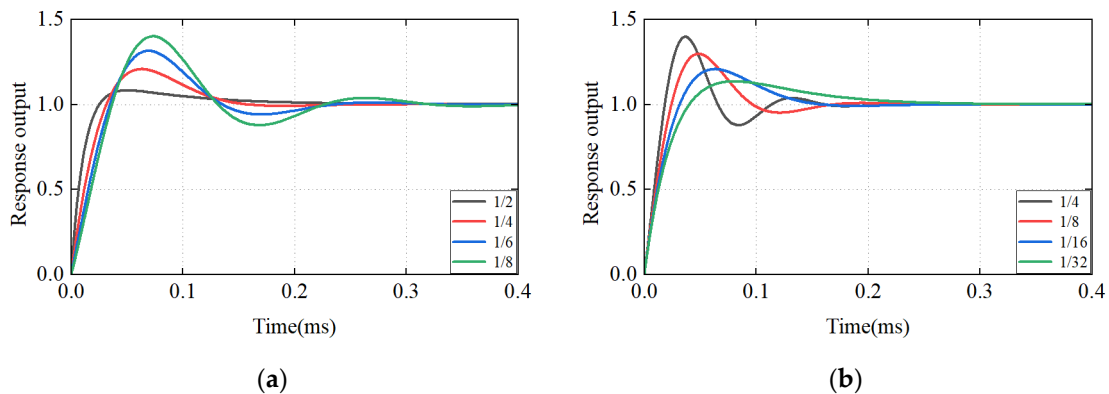


Figure 6. Different parameter settings yield distinct step response curves for the system. (a) $K_I = 1/16$, K_P changes; (b) $K_P = 1/4$, K_I changes.

When K_I is constant, a larger K_P leads to better system stability and faster locking speed. According to Equation (31), an excessively large K_P results in a large damping ratio. According to Equation (32), the natural angular frequency remains constant in this case. Therefore, an excessively large K_P makes the system overly sensitive to noise in the input signal. When K_P is constant, a larger K_I leads to faster system response, but the stability margin decreases. According to Equation (31), an excessively large K_I results in a small damping ratio, leading to excessive overshoot in the system.

According to the analysis above, when the phase error is large, a larger K_P should be chosen, while K_I should be kept relatively small. Preliminary phase adjustment is mainly

achieved by the proportional element, which both ensures response speed and avoids excessive overshoot. When the phase error is small, a smaller K_p should be chosen, while K_i should be larger. This ensures quick elimination of the steady-state error introduced by the proportional element after preliminary phase adjustment.

Figure 7 shows the curves depicting the variation of the phase difference φ and electromagnetic-force F_{z_dc} with the switching frequency f . It can be seen from the figure that when the changing range of switching frequency is $\nabla f = \pm 10$ kHz, the electromagnetic-force of the receiving coil is in a generally monotonic state. Moreover, during this range, the system’s power transfer meets the required specifications.

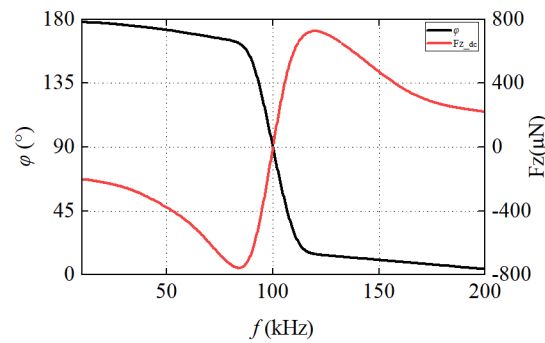


Figure 7. Curve depicting the variation of the phase difference φ with the switching frequency f .

Therefore, to control the impact of electromagnetic-forces on the receiving coil, the objective can be achieved by adjusting the working frequency.

4. Simulation and Experimental Verification

Through modeling and simulation, we analyze the influence of each parameter on the electromagnetic-force F_{z_dc} .

4.1. Simulation Analysis

In order to illustrate the influence of electromagnetic-force generated in the receiving coil during WPT, 3D modeling of the transmitting and receiving coils was conducted using ANSYS Maxwell 2021 R2 finite element software. The coil model is shown in Figure 8a, and the outer circuit of the coil is shown in Figure 8b.

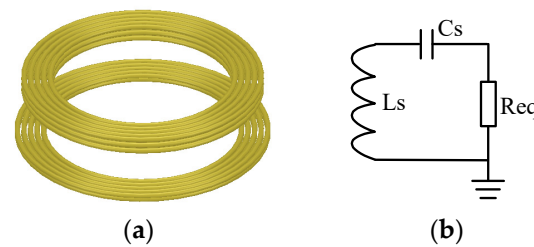


Figure 8. Simulation model. (a) Coil model; (b) External circuit.

The simulation emulates the actual circuit, and the parameters for the simulation setup are listed in Table 2, below. I_p represents the peak current of the transmitting coil, and the coil material is copper.

Table 2. Simulation model parameters.

Coil	Input Excitation (A)	Outside Diameter (mm)	Number of Turns
Transmitting	$I_p \cdot \sin(2\pi\omega t)$	190	10
Receiving	External circuit	190	15

The simulation procedure consisted of three stages: (1) A 3D field simulation was performed to find the magnetic field distribution and induced voltage. (2) The induced secondary current was simulated using the circuit simulator in consideration of the WPT circuit and the switching frequency was adjusted to the maximum current of the receiving coil. (3) The propulsion forces were simulated using a 3D field solver, again based on the induced current from the circuit simulation and incident magnetic field from the primary coil L_p .

The simulation was configured with I_p set to 20 A and a switching frequency of 100 kHz. The variables being scanned are h and L , where h represents the axial separation at the coil’s center along the Z-axis, and L represents the eccentricity along the X-axis.

Figure 9a,b, respectively, show the variation curves of the electromagnetic-force experienced by the receiving coil under different transmission distances and eccentricities. From Figure 9a, it can be observed that as the transmission distance increases, the induced current in the receiving coil gradually decreases, leading to a reduction in the electromagnetic-force. The farther the transmission distance, the less electromagnetic-force interference. In Figure 9b, when there is a lateral displacement in the receiving coil, the change in electromagnetic-force is relatively small.

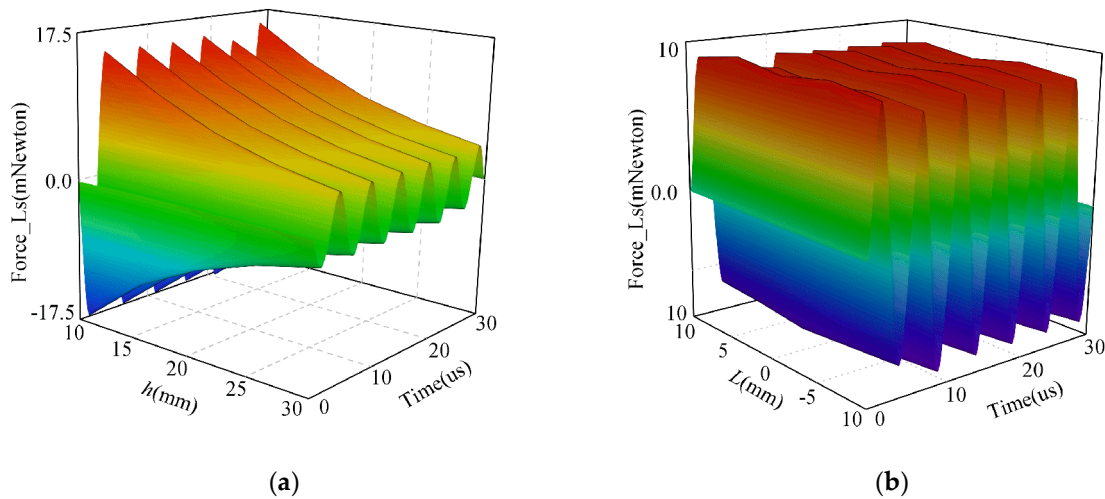


Figure 9. Electromagnetic force experienced by the receiving coil at $f = 100$ kHz. (a) Varying h , $L = 0$ mm; (b) $h = 0$ mm, varying L .

Figure 10 indicates that the frequency of the electromagnetic-force on the receiving coil is twice that of the current’s frequency.

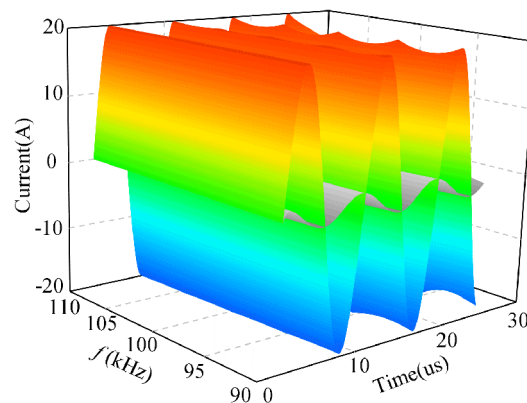


Figure 10. Current curves of the transmitting and receiving coils as the frequency varies.

From Figure 11, it can be observed that at a fixed switching frequency, the electromagnetic-force experienced by the receiving coil gradually decreases to zero as the transmission

distance increases, and then gradually increases. However, when operating in variable frequency mode, as the transmission distance changes, the electromagnetic-force experienced on the receiving coil under different switching frequencies evinces a zero-point phenomenon, that is, the electromagnetic-force is zero.

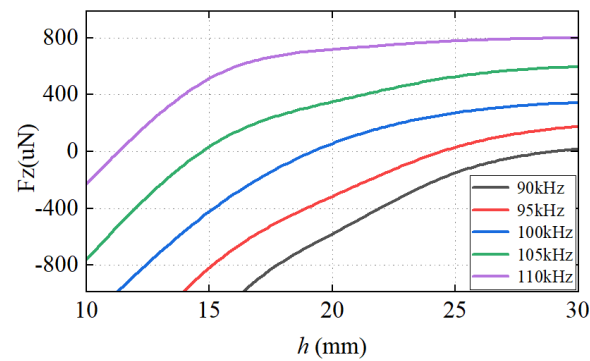


Figure 11. Variation curves of electromagnetic force with frequency and distance.

In Figure 12, when the receiving coil undergoes lateral displacement, the electromagnetic-force it experiences remains at the μN level. As the eccentricity approaches the system's switching frequency, the electromagnetic-force caused by eccentricity becomes smaller.

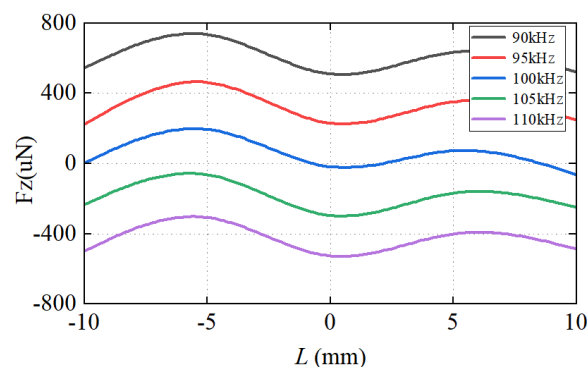


Figure 12. Variation curves of electromagnetic force with frequency and eccentricity.

In summary, by adjusting the switching frequency f of WPT, the interference of the electromagnetic-force on the receiving coil can be effectively reduced, so that the electromagnetic-force can be kept at the order of μN .

4.2. Experimental Verification

In order to verify the influence of electromagnetic-force on the receiving coil, a mechanical torsion test was conducted in the Microgravity Laboratory of the Chinese Academy of Sciences. The experimental device is shown in Figure 13.

Testing was conducted using a torsion balance and a laser rangefinder, with the testing precision reaching the level of 10^{-7} m. To reduce the high-frequency internal resistance caused by the skin effect in the coil, Litz wire winding was employed in the coupler's coil. Since the highest quality factor Q was measured at the resonant frequency of 100 kHz, the matching capacitance for both the transmitting and receiving coils was tuned to 100 kHz. In order to enhance the efficiency of WPT and achieve soft-switching characteristics, the operating frequency was set slightly higher than the resonant frequency.

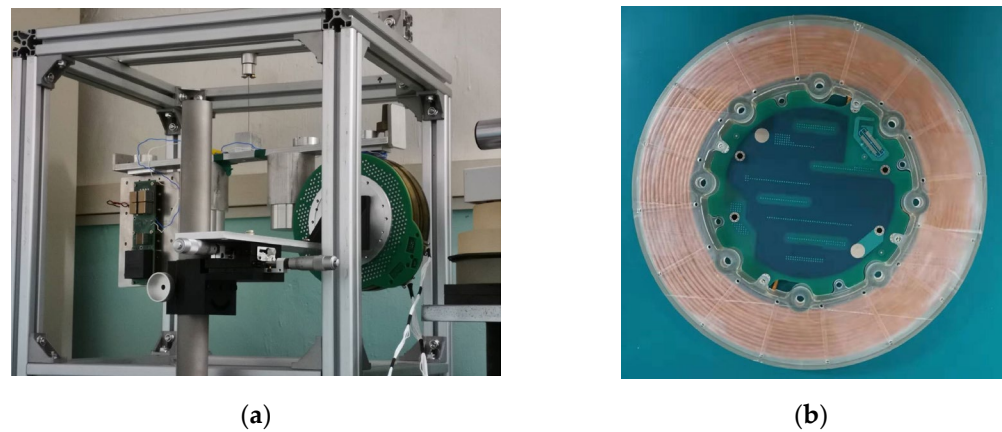


Figure 13. Torsion weighing test platform. (a) Experimental platform; (b) Coil.

The detailed parameters of the coil are provided in Table 3.

Table 3. Parameters of a WPT coil.

Parameter	Primary Coil	Secondary Coil
Diameter	190 mm	190 mm
Turns of coil	10	15
Weight	0.21 kg	0.33 kg
Self-inductance	23.462 μ H	53.288 μ H
Mutual inductance	$h = 10$ mm	16.9 μ H
	$h = 20$ mm	13.02 μ H
	$h = 30$ mm	9.44 μ H

(1) The magnitude of electromagnetic force on the receiving coil at different positions

In Figure 14a,b, it can be observed that at a transmission distance of 10 mm, the electromagnetic-force on the receiving coil is repulsive, and the electromagnetic-force F_{z_dc} is about -387μ N, with a switching frequency of 109.6 kHz. When the eccentricity is 10 mm, the electromagnetic-force is about -480μ N, and the system's switching frequency is 108.6 kHz.

In Figure 14c,d, it can be observed that at a transmission distance of 20 mm, the electromagnetic-force on the receiving coil is repulsive, and the electromagnetic-force F_{z_dc} is about -113μ N, with a switching frequency of 101.3 kHz. When the eccentricity is 10 mm, the electromagnetic-force is about -143μ N, and the system's switching frequency is 98.6 kHz.

In Figure 14e,f, it can be observed that at a transmission distance of 30 mm, the electromagnetic-force on the receiving coil is attractive, and the electromagnetic-force F_{z_dc} is about 148 μ N, with a switching frequency of 91.7 kHz. When the eccentricity is 10 mm, the electromagnetic-force is about 162 μ N, and the system's switching frequency is 90.8 kHz.

Table 4 presents a comparison between simulation-based and experimental data as to the electromagnetic-force magnitude exerted on the receiving coil at various positions.

Due to the presence of magnetic shielding materials around the coupled coils, as well as the influence of circuit boards and mounting metal surfaces, the electromagnetic-force is further affected. Additionally, there may be errors in the actual transmission distance h measured using laser rangefinder sensors. Therefore, there will be slight differences between simulation and experimentation.

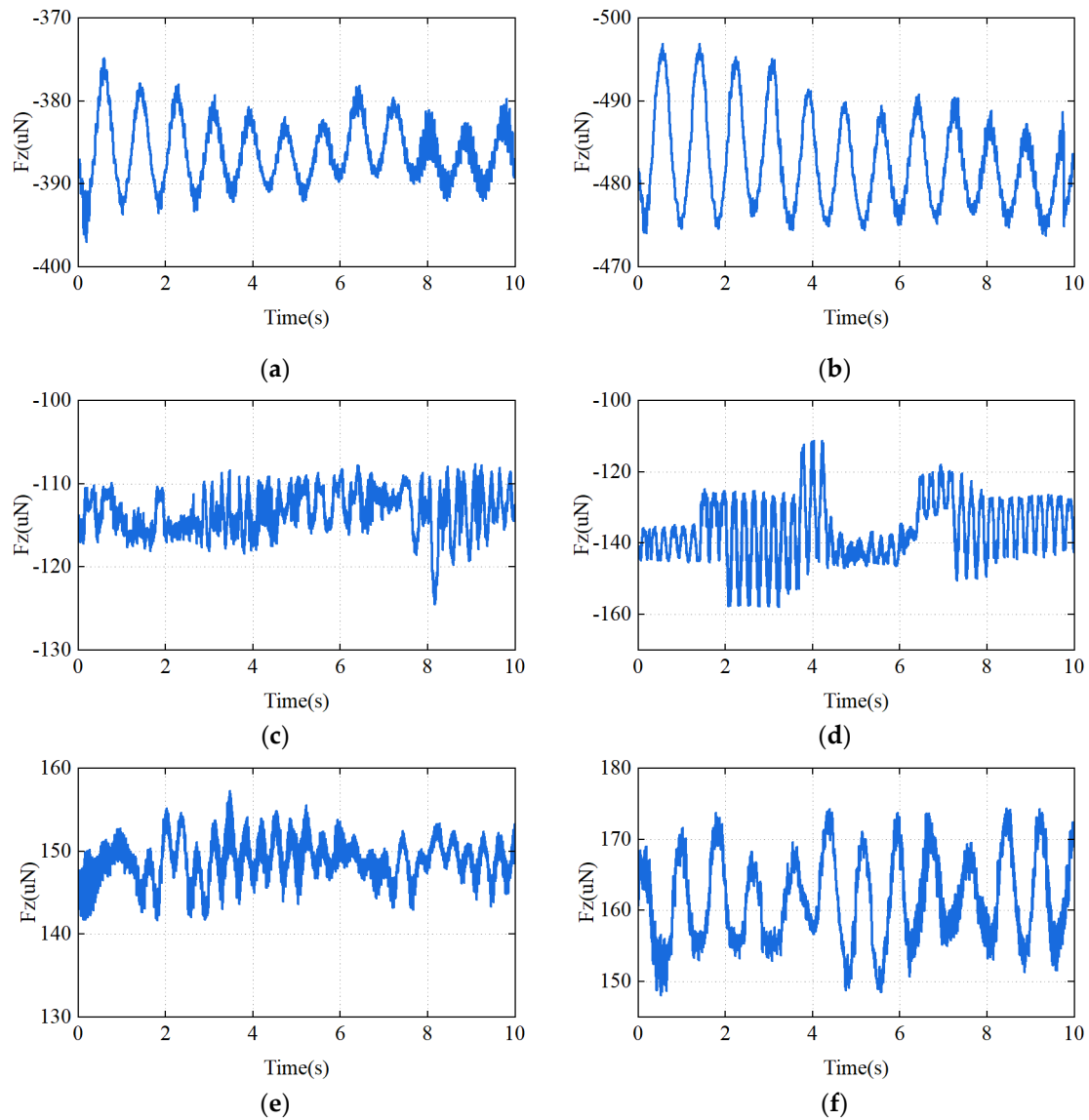


Figure 14. The magnitude of the electromagnetic force on the receiving coil at different transmission distances. (a) $h = 10$ mm, $L = 0$ mm; (b) $h = 10$ mm, $L = 10$ mm; (c) $h = 20$ mm, $L = 0$ mm; (d) $h = 20$ mm, $L = 10$ mm; (e) $h = 30$ mm, $L = 0$ mm; (f) $h = 30$ mm, $L = 10$ mm.

Table 4. Simulation-based and experimental results.

Position		Simulation		Experimental	
L (mm)	h (mm)	F_{z_dc} (μ N)	f (kHz)	F_{z_dc} (μ N)	f (kHz)
0	10	−318	110	−387	109.6
	20	−45	100	−113	101.3
	30	119	90	148	91.7
10	10	−469	110	−480	108.6
	20	−130	100	−143	98.6
	30	154	90	162	90.8

In the coaxial scenario, when the transmission distance h is minimal, the electromagnetic-force exerted on the receiving coil is at its maximum and repulsive. At this point, the system’s switching frequency is also at its maximum value. As h increases, the repulsive force on the receiving coil decreases until, at a certain position, the receiving coil is no longer affected by electromagnetic-force, and the phase difference is 90° . At this point, the

switching frequency of the switches is at the rated value. As h is further increased, the electromagnetic-force on the receiving coil becomes attractive, and the greater h becomes, the more the attractive force increases. When the transmission distance reaches its maximum, the attractive force on the receiving coil also reaches its maximum, and the system's switching frequency is minimized.

When the transmission distance is fixed, any deviation in the x or y direction by the receiving coil results in an increase in the electromagnetic-force exerted on it, causing a slight decrease in the system's switching frequency. As the transmission distance increases, the impact of the deviation on the electromagnetic-force diminishes.

In summary, when the levitator is in free drift, adjusting the system's switching frequency f ensures that the electromagnetic-force interference on the receiving coil is less than 500 μN , meeting the experimental requirements of space science.

(2) Power and efficiency curves

The experiment was conducted in the levitation laboratory. The test results of WPT under the full-load conditions are shown in Figure 15, when the transmission distance is 10 mm, the transmission power of the system is 98 W; when the transmission distance is 30 mm, the output power is 85 W. The system demonstrated a maximum efficiency of 78%, meeting the power supply requirements of the levitation system.

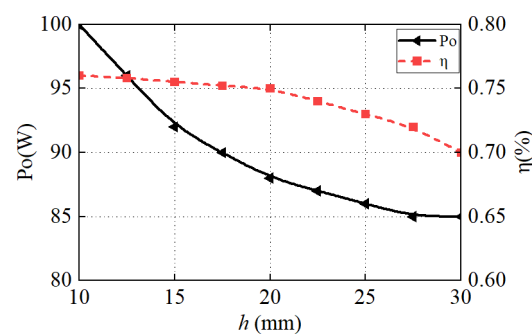


Figure 15. Power and efficiency curves of WPT at the rated state.

5. Discussion

To mitigate the electromagnetic-force interference within the high-microgravity experimental cabinet during WPT, the research described utilizes adjustments to the system's switching frequency to control the magnitude and direction of the electromagnetic-force. However, it is noted that further discussion is required regarding the effectiveness of this method, based on theoretical analysis and experimental findings.

(1) Otherness

Compared to the method of adjusting the capacitance of the receiving coil, as described in [10], this paper's approach of adjusting the system's switching frequency enables real-time control of the magnitude and direction of the electromagnetic-force on the receiving coil. This effectively avoids the need for real-time changes to the resonant capacitance of the receiving end, thus enhancing the system's flexibility. Although the research described in [20] reduces the electromagnetic-force on the receiving coil to zero, it does not fulfill other requirements of the space-based high-precision experimental cabinet.

(2) Limitations

Small variations in transmission distance directly affect the magnitude and direction of the electromagnetic-force, imposing strict requirements on the measurement of the receiving coil's position. The more accurately the transmission distance is measured, the more precise the control of the magnitude and direction of the electromagnetic-force, resulting in smaller errors. Additionally, as the transmission distance increases, it is necessary to reduce the switching frequency, leading to a decrease in the overall transmission power

and efficiency of the system. Therefore, this method is suitable for scenarios in which the transmission distance varies within the range of millimeters and where there are no stringent requirements on power and transmission efficiency.

(3) Future research direction

WPT is a current research hotspot and has found wide application in many fields. Research related to this technology primarily focuses on improving transmission power and efficiency. However, studies on the electromagnetic-force interference generated during WPT are relatively scarce. It is worth contemplating and researching how to reduce the impact on surrounding electronic devices during the power supply process.

6. Conclusions

In order to reduce electromagnetic-force interference caused by the free drift of the receiving coil in WPT systems, this paper proposes a method of adjusting the switching frequency to control the magnitude and direction of the electromagnetic-force on the receiving coil. When the transmission distance changes, the actual transmission distance is measured using a laser ranging sensor, and the system's switching frequency is dynamically adjusted, effectively reducing the impact of the electromagnetic-force on the receiving coil. Experimental results demonstrate that as the transmission distance changes from 10 mm to 30 mm, the system's switching frequency changes from 109.6 kHz to 90.8 kHz, and the electromagnetic-force on the receiving coil changes from $-387 \mu\text{N}$ to $148 \mu\text{N}$. Therefore, the feasibility of the control method has been verified through simulation and experiment, and the influence of the electromagnetic-force can meet the requirements of a high-microgravity experimental cabinet, which lays a theoretical and experimental basis for the application of WPT technology in space stations.

Author Contributions: Conceptualization, Y.H. and W.D.; Methodology, Y.H.; Software, X.L. and L.M.; Validation, L.M.; Investigation, Y.H. and W.D.; Resources, W.D., X.L. and H.Z.; Data curation, L.M.; Writing—original draft, Y.H.; Writing—review & editing, Y.H., W.D. and X.L.; Visualization, L.M.; Supervision, W.D. and H.Z.; Project administration, W.D. and X.L.; Funding acquisition, X.L. All authors have read and agreed to the published version of the manuscript.

Funding: This research was funded by the Chinese Manned Space Program—Space Utilization System (412021000031) and National Key Research and Development Program of China (2022YFB3604004).

Data Availability Statement: The data presented in this study are available in this article.

Conflicts of Interest: The authors declare no conflict of interest.

References

1. Zhang, Z.; Pang, H.; Georgiadis, A.; Cecati, C. Wireless power transfer—An overview. *IEEE Trans. Ind. Electron.* **2018**, *66*, 1044–1058. [[CrossRef](#)]
2. Patil, D.; McDonough, M.K.; Miller, J.M.; Fahimi, B.; Balsara, P.T. Wireless power transfer for vehicular applications: Overview and challenges. *IEEE Trans. Transp. Electr.* **2018**, *4*, 3–37. [[CrossRef](#)]
3. Xu, F.; Wong, S.C.; Chi, K.T. Overall loss compensation and optimization control in single-stage inductive power transfer converter delivering constant power. *IEEE Trans. Power Electron.* **2021**, *37*, 1146–1158. [[CrossRef](#)]
4. Ming, X.; Qingxin, Y.; Pengcheng, Z.; Jianwu, G.; Yang, L. Application status and key issues of wireless power transmission technology. *Trans. China Electrotech. Soc.* **2021**, *36*, 1547–1568.
5. Gao, M.; Zhao, G.; Gu, Y. Recent progress in space science and applications of China's space station in 2020–2022. *Chin. J. Space Sci.* **2022**, *42*, 503–510. [[CrossRef](#)]
6. Wang, S.K.; Wang, K.; Zhou, Y.L.; Yan, B.; Li, X.; Zhang, Y.; Wang, A.P. Development of the varying gravity rack (VGR) for the Chinese space station. *Microgravity Sci. Technol.* **2019**, *31*, 95–107. [[CrossRef](#)]
7. Zhang, Y.; Dong, S.; Wang, K.; Zhou, Y.; Sheng, Q.; Tan, H. Design, simulation and test of thermal control system of centrifuge for space utilization. *Microgravity Sci. Technol.* **2020**, *32*, 761–772. [[CrossRef](#)]
8. Hu, Y.; Li, X.; Dong, W.; Zhang, H.; Wang, X. The application progress of wireless power transfer in space utilization field. In Proceedings of the 2023 International Conference on Wireless Power Transfer (ICWPT), Weihai, China, 13–15 October 2023; pp. 520–532.

9. Kim, D.; Kim, M.; Yoo, J.; Park, H.; Ahn, S. Magnetic resonant wireless power transfer for propulsion of implantable micro-robot. *J. Appl. Phys.* **2015**, *117*, 17E712. [[CrossRef](#)]
10. Kim, D.; Park, J.; Park, H.H.; Ahn, S. Generation of magnetic propulsion force and torque for microrobot using wireless power transfer coil. *IEEE Trans. Magn.* **2015**, *51*, 8600104. [[CrossRef](#)]
11. Kim, D.; Hwang, K.; Park, J.; Park, H.H.; Ahn, S. Miniaturization of implantable micro-robot propulsion using a wireless power transfer system. *Micromachines* **2017**, *8*, 269. [[CrossRef](#)] [[PubMed](#)]
12. Kim, D.; Ahn, S. Wireless Power Transfer-Based Microrobot with Magnetic Force Propulsion Considering Power Transfer Efficiency. *J. Electromagn. Eng. Sci.* **2022**, *22*, 488–495. [[CrossRef](#)]
13. Narayanamoorthi, R.; Juliet, A.V.; Chokkalingam, B. Frequency splitting-based wireless power transfer and simultaneous propulsion generation to multiple micro-robots. *IEEE Sens. J.* **2018**, *18*, 5566–5575. [[CrossRef](#)]
14. Song, S.; Song, S.; Meng, M.Q.H. Electromagnetic actuation system using stationary six-pair coils for three-dimensional wireless locomotive microrobot. In Proceedings of the 2017 IEEE International Conference on Information and Automation (ICIA), Macau, China, 18–20 July 2017; pp. 305–310.
15. Zhang, Q.; Song, S.; Song, S. Study on magnetic field model of independent circular coils for wireless manipulation of microrobots. In Proceedings of the 2017 IEEE International Conference on Information and Automation (ICIA), Macau, China, 18–20 July 2017; pp. 1137–1142.
16. Zhang, X.; Ren, Y.; Sha, L.; Yang, Q.; Ni, X.; Wang, F. Analysis of dynamic characteristics of foreign metal objects under electromagnetic force in high-power wireless power transfer. *Energies* **2020**, *13*, 3881. [[CrossRef](#)]
17. Zhang, X.; Ni, X.; Wei, B.; Wang, S.; Yang, Q. Characteristic analysis of electromagnetic force in a high-power wireless power transfer system. *Energies* **2018**, *11*, 3088. [[CrossRef](#)]
18. Zhang, X.; Wang, F.; Ni, X.; Ren, Y.; Yang, Q. Structure electromagnetic force analysis of WPT system under fault conditions. *IEEE Access* **2020**, *8*, 152990–153000. [[CrossRef](#)]
19. Zhang, X.; Yuan, Z.; Yang, Q.; Li, Y.; Zhu, J.; Li, Y. Coil design and efficiency analysis for dynamic wireless charging system for electric vehicles. *IEEE Trans. Magn.* **2016**, *52*, 8700404. [[CrossRef](#)]
20. Guo, S.Z. Research on Inductively Coupled Wireless Power Supply Technology with Perturbation Force. Ph.D. Thesis, Xidian University, Xi'an, China, 2019.
21. Han, G.; Wei, Y.; Yan, L. Analysis of electromagnetic force on wireless charging structure. *Wirel. Netw.* **2023**, 1–10. [[CrossRef](#)]
22. Babic, S.I.; Akyel, C. Magnetic force calculation between thin coaxial circular coils in air. *IEEE Trans. Magn.* **2008**, *44*, 445–452. [[CrossRef](#)]

Disclaimer/Publisher's Note: The statements, opinions and data contained in all publications are solely those of the individual author(s) and contributor(s) and not of MDPI and/or the editor(s). MDPI and/or the editor(s) disclaim responsibility for any injury to people or property resulting from any ideas, methods, instructions or products referred to in the content.